IOP Publishing Nanotechnology
Nanotechnology **20** (2009) 235307 (10pp) doi:10.1088/0957-4484/20/23/235307

Directional growth of metallic and polymeric nanowires

Prem S Thapa[1,3], **Bruce J Ackerson**[1], **Daniel R Grischkowsky**[2] and **Bret N Flanders**[1,3,4]

[1] Department of Physics, Oklahoma State University, Stillwater, OK 74078-3072, USA
[2] School of Electrical and Computer Engineering, Oklahoma State University, Stillwater, OK 74078, USA

E-mail: bret.flanders@phys.ksu.edu

Received 3 February 2009, in final form 26 March 2009
Published 18 May 2009

Abstract

This work delineates the mechanism by which directional nanowire growth occurs in the *directed electrochemical nanowire assembly* (DENA) technique for growing nanowires on micro-electrode arrays. Indium, polythiophene, and polypyrrole nanowires are the subjects of this study. This technique allows the user to specify the growth path without the use of a mechanical template. Nanowire growth from a user-selected electrode to within ±3 μm of the straight line path to a second electrode lying within a $\sim 140°$ angular range and a ~ 100 μm radius of the selected electrode is demonstrated. Theory for one-dimensional electrochemical diffusion in the inter-electrode region reveals that screening of the applied voltage is incomplete, allowing a long range voltage component to extend from the biased to the grounded electrode. Numerical analysis of two-dimensional multi-electrode arrays shows that a linear ridge of electric field maxima bridges the gap between selected electrodes but decays in all other directions. The presence of this anisotropic, long range voltage defines the wire growth path and suppresses the inherent tip splitting tendency of amorphous polymeric materials. This technology allows polythiophene and polypyrrole to be grown as wires rather than fractal aggregates or films, establishing DENA as an on-chip approach to both crystalline metallic and amorphous polymeric nanowire growth.

1. Introduction

Precise nanowire growth techniques are vital to nanoelectronics-development. One seeks control over the wire composition, dimensions, and growth direction in a single approach. This has been an elusive goal. Templated growth is in broad-use as the wire-compositions can be metallic [1], semiconductor, or polymeric [2, 3]. The wire-shapes are reproducible [4], and the output is scalable. However, prefabrication of mechanical growth channels and post-growth release of the wires are typically required. Methods for circumventing these laborious steps are, therefore, sought. Dielectrophoretic assembly is a template-free approach that uses a voltage to chain metallic or semiconductor particles into wires in the gaps between electrodes [5–9], but these nanoparticulate materials suffer from resistivities several orders of magnitude in excess of bulk metals [6, 9]. The vapor–liquid–solid (VLS) technique does not require growth channels and produces single crystalline wires in high yield [10, 11]. VLS is especially useful for semiconductor–nanowire assembly. However, this approach can only fabricate crystalline materials. Conducting polymeric nanowires are amorphous materials that are needed for basic transport studies [12, 13] and sensor-applications [14, 15] and are also promising electrophysiological materials [16, 17]. The wire-lengths that are attainable in most approaches to polymeric wire growth are limited to 10 μm or less [14, 18]. Dip-pen lithography relaxes the wire-length constraint [19], but is restricted to applications where the use of a scanning probe is feasible. In response to the need for precise nanowire growth techniques, the present work delineates methodology for the directional growth of both crystalline metallic wires and amorphous polymeric wires between user-selected sites in on-chip circuitry. A letter reporting the basic capabilities of this methodology has been published elsewhere [20].

---

[3] Present address: Department of Physics, Kansas State University, Manhattan, KS 66506-2601, USA.

[4] Author to whom any correspondence should be addressed.

0957-4484/09/235307+10$30.00

The technique of *directed electrochemical nanowire assembly* (DENA) permits the template-free, growth of near single crystalline metallic nanowires from aqueous salt solutions [21–23]. The wires may be grown from Co, Ni, Au [22], Ag, Pd, Pt [24], In [21], or Pb. Their diameter is tunable across the 40 nm–2 μm range [23]. DENA enables the growth of amorphous polypyrrole or polythiophene nanowires, as well [20]. *The growth path of DENA-fabricated wires is predictable*; it follows the line connecting the tips of a selected electrode pair across distances as large as 100 μm. The origin of this control requires elucidation because this capability enables fabrication of *electrode–nanowire–electrode* assemblies—structures that are of use in the characterization of nanowire-transport properties. For example, we have used this technique to fabricate assemblies with electrode–wire contact resistances of only ~10 Ω [22]. Small contact resistances are required before the nanowire-conductivity may be studied, as the contact properties can overwhelm the transport properties of the wire [25]. Additionally, we have used these assemblies to measure the conductivities of polypyrrole wires (0.5 ± 0.3 S cm^{-1}) and of polythiophene wires (7.6 ± 0.8 S cm^{-1}) [20]. Finally, the directional growth capability yields a single-step approach to interconnecting laboratory instrumentation with biological cells or other submicron targets to which the wires are grown [20].

The metallic structures produced by DENA range from needle-shaped wires to highly branched tree-like deposits [21–23], two signature-structures of the *dendritic solidification* mechanism [26]. Indeed, this diffusion limited process figures prominently in the DENA technique [27, 28]. Dendritic solidification pervades alloy crystallization, solidification from supercooled melts [29] and supersaturated solutions [30], and electrochemical deposition [31, 32, 23]. It underlies snowflake formation [33–36] and bears a fundamental similarity to viscous fingering in hydrodynamics due to the isomorphism between the diffusion and the Navier–Stokes equations [37, 38]. Thus, it is a widely studied and well understood process. The *surface tension anisotropy* of the advancing dendrite plays a key role in this process: the dendrite grows in the direction normal to its crystallographic plane of maximum surface energy, and it does so in a shape preserving manner [39]. See the appendix for a more complete explanation of shape preserving growth. Dendrites grow in the direction of maximum surface energy because the particle deposition rate along this vector exceeds that of any other direction. With no structural anisotropy, the attachment kinetics is the same at all points of common curvature along the front, so the growth-axis is ill-defined.

In light of these physics, one would expect amorphous materials to split into multiple tips during their growth, as such materials lack crystallographic growth-axes. For example, a 2D bubble blown from a central point in a Hele-Shaw cell grows analogously to diffusion limited growth [40]. The surface tension of the gas–liquid interface is isotropic, and the bubble grows isotropically—its circular front splits into numerous fingers that advance radially outward, but without any angular preference. Isotropic growth is also observed in Au atom aggregation on cold surfaces, where the Au surface energy does not play a significant role. The resulting highly branched Au aggregates have fractal dimensions of 1.7 [41]. Such structures are not wire-like—they do not grow along linear paths. Study is warranted, therefore, to elucidate the curious result that DENA produces wire-like structures from polypyrrole and polythiophene without the use of mechanical templates; the growth occurs along predictable and linear inter-electrode paths [20]. Both of these conducting polymers are amorphous materials with zero crystalline anisotropy. Their natural tendency is to grow non-directionally, yielding highly ramified, filamentous structures. Yet this is not observed.

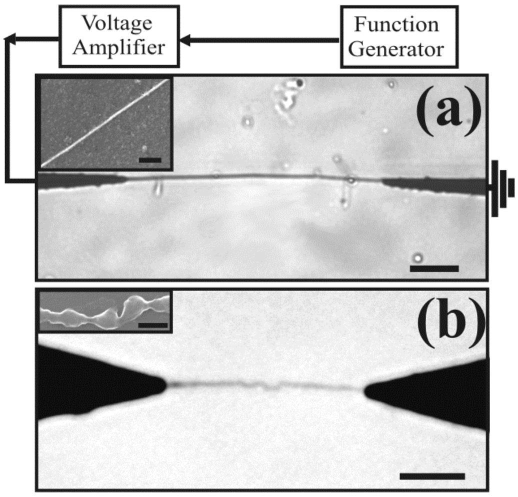

Figure 1. (a) Apparatus for the DENA technique. The optical micrograph depicts an In wire grown between the electrode tips. The scale bar denotes 10 μm. Inset. A scanning electron micrograph of an In nanowire. The scale bar denotes 250 nm. (b) An optical micrograph of a DENA-grown polythiophene wire. The scale bar denotes 10 μm. Inset. A scanning electron micrograph of a polythiophene nanowire. The scale bar denotes 100 nm.

The present study articulates the role of the applied electric field in the DENA-based growth of metallic and polymeric nanowires. This property underlies the directional character of metallic and polymeric wire growth. It also underlies DENA's ability to produce wire-like structures from amorphous materials. Because screening of the applied voltage near the solidification front is incomplete, an anisotropic, long range voltage component survives. This component defines a ridge of electric field maxima that extends between selected on-chip electrodes. This electrical ridge defines a growth channel for the wires that is analogous to the mechanical channels of templated nanowire growth techniques. Metallic dendrites crystallize almost exclusively along these channels. The user thereby controls their growth path in the laboratory frame. Amorphous materials electrochemically polymerize along this channel at higher rates than outside of the channel. The channel thereby constrains the isotropic growth tendency, producing wire-like structures from amorphous materials.

2. Experimental details

2.1. Indium wire growth

The experimental apparatus for the DENA technique is shown in figure 1(a), consisting of sharp, transiently biased electrodes immersed in concentrated salt solution. This apparatus is described in detail elsewhere [21]. The optical micrograph in this figure depicts an indium nanowire spanning the 60 μm gap between the ends of a tapered electrode pair. The electrodes were deposited in 12-pair arrays on quartz substrates using standard lithographic techniques [9] and are composed of 100 nm thick base layers of Ti and 500 nm thick top-layers of Al. The wire in this micrograph was grown by depositing a 10 μl aliquot of aqueous 0.055 M In(CH$_3$COO)$_3$ solution across the electrodes and applying an ±18 V square-wave with a 1.0 MHz frequency and a 50% duty cycle to the left electrode while the right electrode was grounded. Growth does not occur when voltage–amplitudes less than 18 V are used. A *square*-waveform is optimal, as sinusoidal or sawtooth waveforms require larger voltage–amplitudes to induce growth (>40 V). Presumably, square-waves are more effective because they apply the full voltage for (nearly) the entire half-period, whereas sine waves reach their full amplitude for only an instant during their half-cycle. Duty cycles not equal to 50% result in rapid electrode-dissolution, preventing wire growth. The frequency of the alternating voltage may be varied between 0.5 and 3.5 MHz for In wire growth. This degree-of-freedom provides sensitive control over the growth velocity and wire-diameter (across the 100 nm–1 μm range) [23]. Electron diffraction was used to identify the wire composition as indium [21]. The scanning electron micrograph in the inset depicts a smooth cylindrical wire with a diameter of 106 nm. To collect this image, the wire laden electrode array was mounted directly in the instrument.

2.2. Polythiophene wire growth

A full description of the DENA-based growth of polymeric nanowires is published elsewhere [20]. The same set-up described above for metallic wire growth was used for the growth of the polythiophene wires in this study. A typical polymeric electrode–wire–electrode assembly is shown in figure 1(b). A 10 μl aliquot of aqueous solution containing 0.01 M ethylenedioxy-thiophene (EDOT) and 0.02 M poly(sodium styrene sulfonate) (PSS) was deposited across the electrodes. A square-wave voltage-signal (±2.5 V, 100 kHz) was used to induce wire growth across the 30.2 μm gap in figure 1(b). Growth across gaps as large as 100 μm is straight-forward. The composition of the polythiophene wire was verified by micro-Raman spectroscopy [20]. The inset depicts a scanning electron micrograph of the wire. Its structure is knobby, varying from 98 to 669 nm in thickness with a lengthwise averaged diameter of 340 nm.

2.3. Polypyrrole wire growth

Polypyrrole wires were grown on the same electrode arrays. A 10 μl aliquot of aqueous solution containing 0.50 M freshly distilled pyrrole and 0.50 M sodium dodecyl sulfate was deposited across the electrodes. A ±2.5 V, 100 kHz square-wave voltage-signal was used to induce growth. Micro-Raman spectroscopy was used to determine the polypyrrole wire composition [20].

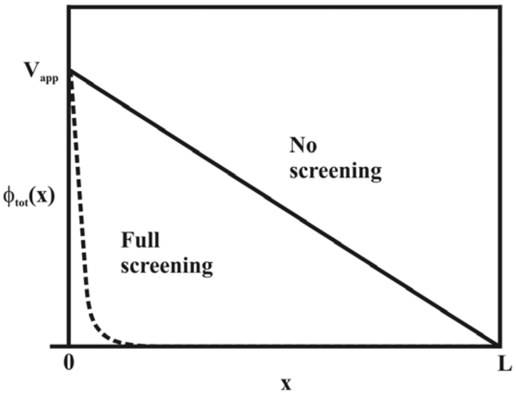

Figure 2. Potential profiles $\phi(x)$ for the cases of no screening (solid line) and full screening (dashed line) of a voltage V_{App} that is applied to the left wall of the cell. The right wall is grounded.

3. Theory

The growth path of both the metallic and polymeric wires is well described by the straight line that connects the tips of the alternating and grounded electrodes. How does the applied voltage influence the growth path? Consider the gap between two parallel electrode-plates. A voltage V_{App} is applied to one electrode positioned at $x = 0$. The other positioned at $x = L$ is grounded. The solid line in figure 2 denotes the voltage profile corresponding to a rightward directed uniform electric field (V_{App}/L) in the inter-electrode gap. If the medium between the electrodes is electrolytic, ions near the biased electrode will respond to the applied voltage by rearranging to screen the electrode-potential over a short (<10 nm) distance. This ion-sheath surrounding the electrode is called a Helmholtz layer and is analogous to Debye–Hückel screening of point charges in solution [42, 43]. The dashed line in figure 2 illustrates the voltage profile when there is complete screening. A combination of the processes corresponding to the solid and dashed profiles of figure 2 must be considered if redox chemistry and deposition occur at the electrodes, as in DENA. Below we present a theory for partial screening and relate this theory to the directional growth and the amorphous wire-fabrication capabilities of the DENA technique.

We consider the one-dimensional motion of ions in solution in response to an externally applied electric field. We assume the body forces on the solution are sufficiently small that convection is negligible: we need not include hydrodynamics. We consider continuity equations for each of the charged species. For simplicity we assume a single positive and single negative species; the effects of metallic ions that have dissociated from unbiased electrodes are neglected [42]. The two continuity equations (conservation of species-type) are

$$\partial_t C_1(x,t) = -\nabla \cdot \vec{j}_1(x,t) \qquad (1a)$$

and

$$\partial_t C_2(x,t) = -\nabla \cdot \vec{j}_2(x,t)\,. \qquad (1b)$$

Here $C_1(x,t)$ and $C_2(x,t)$ are the spatially dependent concentrations of the positive and negative ions, respectively, and $j_1(x,t)$ and $j_2(x,t)$ are the local fluxes of these species.

The fluxes are written in terms of concentration gradients $\nabla C_i(x,t)$ and electric forces $z_i eE(x,t)$ acting on the species, where $E(x,t)$ is the electric field and z_i is the valence of species i:

$$j_1(x,t) = -D_1\nabla C_1(x,t) + \beta D_1 z_1 eE(x,t)\,C_1(x,t) \quad (2a)$$

and

$$j_2(x,t) = -D_2\nabla C_2(x,t) - \beta D_2 z_2 eE(x,t)\,C_2(x,t)\,. \quad (2b)$$

D_1 and D_2 are the diffusion constants of the cationic and anionic species, respectively, and e is 1.602×10^{-19} C, and β is the inverse thermal energy $(k_{\mathrm{B}}T)^{-1}$ where k_{B} is Boltzmann's constant and T is the temperature. The Poisson equation describes the electric potential $\phi(x,t)$ due to net charge at position x and time t:

$$\nabla^2\phi(x,t) = -\frac{e}{\varepsilon\varepsilon_0}\left[z_1C_1(x,t) - z_2C_2(x,t)\right]. \quad (2c)$$

ε_0 is the permittivity of free space (8.854×10^{-12} C^2 N^{-1} m^{-2}), and ε is the dielectric constant of water (80). The spatial and temporal dependences of the quantities j_i, C_i, E, and ϕ will be implicit for the remainder of this section. For simplicity, we consider a monovalent salt, so $z_1 = z_2 = 1$ and $C_{10} = C_{20} = C_0$. We further assume that $D_1 = D_2 = D$.

Screening will alter the field in the solution with respect to the prescreening field value of $E_0 = V_{\mathrm{App}}/L$ that is present before charge-reorganization occurs. The concentrations will change with respect to their bulk values of C_0, as well. The fluxes j_i are then fractions α of their initial amplitudes $j_{i0} = \beta DeE_0C_0$. After some rearrangement,

$$D\nabla C_1 - \beta De(E_0 - \nabla\phi_1)C_1 = -\alpha j_{10} \quad (3a)$$

and

$$D\nabla C_2 + \beta De(E_0 - \nabla\phi_1)C_2 = \alpha j_{10} \quad (3b)$$

where we used the relationship $j_{10} = -j_{20}$. The new field $-\nabla\phi_1$ accounts for the effect of screening on the initial electric field E_0. The terms in equations (3*a*) and (3*b*) have dimensions of flux (Length^{-2} Time^{-1}). We rescale the coordinates to dimensionless form by multiplying through by factors of $|\beta DeE_0C_0|^{-1}$, the inverse of the initial flux amplitude, yielding

$$\nabla' Y_1 - (1 - \nabla'\psi)Y_1 = -\alpha \quad (4a)$$

and

$$\nabla' Y_2 + (1 - \nabla'\psi)Y_2 = \alpha \quad (4b)$$

where $Y_1 = C_1/C_0$, $Y_2 = C_2/C_0$, and $\psi = \beta e\phi_1$ (all unitless). The notation $\nabla' = \mathrm{d}/\mathrm{d}x'$ denotes $(\beta eE_0)^{-1}\nabla$ and $x' = \beta eE_0x$. Equation (2*c*) is non-dimensionalized by multiplying through by $(\beta eE_0)^{-2}$, yielding

$$\nabla'^2\psi = -\gamma\,(Y_1 - Y_2) \quad (4c)$$

where $\gamma = C_0/(\beta\varepsilon\varepsilon_0E_0^2)$.

Y_1 and Y_2 are not independent but are coupled through their dependence on ψ (equation (4*c*)). To eliminate Y_1 and Y_2 in order to solve for the inter-electrode field, we add and subtract equations (4*a*) and (4*b*) to obtain

$$\nabla'\Lambda - (1 + E_1)\Gamma = 0 \quad (5a)$$

and

$$\nabla'\Gamma - (1 + E_1)\Lambda = -2\alpha, \quad (5b)$$

where $\Lambda = Y_1 + Y_2$, $\Gamma = Y_1 - Y_2$, and $E_1 = -\nabla'\psi$. The Poisson equation becomes

$$\nabla' E_1 = \gamma\Gamma. \quad (5c)$$

Equation (5*a*) is integrated to give

$$\gamma\Lambda = K_1 + \left(1 + \frac{E_1}{2}\right)E_1, \quad (6)$$

where equation (5*c*) was invoked. Substitution of this expression for Λ and equation (5*c*) for Γ into equation (5*b*) obtains a second order non-linear differential equation for E_1.

$$\nabla'^2E_1 - (1 + E_1)\left[K_1 + \left(1 + \frac{E_1}{2}\right)E_1\right] = -2\alpha\gamma. \quad (7)$$

If $\alpha = 1$, there is no screening and $E_1 = 0$; thus, $K_1 = 2\gamma$. If $\alpha < 1$, screening reduces the field in the solution from its initial value V_{App}/L. E_1 accounts for this change due to reorganization of charge densities. Let us further resolve this change by the substitution $E_1 = E_2 + \delta$ which separates the uniform component of the modifying field δ from the position dependent component E_2. Equation (7) expands to

$$\begin{aligned}\nabla'^2E_2 = {}&\left[2\gamma(1-\alpha) + \delta + 2\gamma\delta + \frac{3\delta^2}{2} + \frac{\delta^3}{2}\right]\\ &+ E_2\left(1 + 2\gamma + 3\delta + \frac{3\delta^2}{2}\right)\\ &+ E_2^2\left(\frac{3}{2} + \frac{3\delta}{2}\right) + \frac{E_2^3}{3}.\end{aligned} \quad (8)$$

Setting the bracketed term equal to zero, as $\nabla'^2E_2 = 0$ if $E_2 = 0$, determines δ to be $\delta = \alpha - 1$. This quantity is less than unity, while the parameter γ is of the order of 10^3 (shown below). In this limit, equation (8) is approximated as

$$\nabla'^2E_2 \cong 2\gamma E_2, \quad (9a)$$

a Debye–Hückel form with the general solution

$$E_2\left(x'\right) = A_1\mathrm{e}^{\rho x'} + A_2\mathrm{e}^{-\rho x'} \quad (9b)$$

where $\rho = (2\gamma)^{1/2}$. We equate A_1 to 0 because we expect $x'(L)$ to be 1000s of unitless screening lengths in distance, so $E_2[x'(L)]$ should equal zero. A realistic value for ρ^{-1} is computed in section 4.

We seek the total potential $V_{\mathrm{Tot}}(x)$ at all points in the solution. To recap, the total field E_{Tot} at a given point is $E_{\mathrm{Tot}} = E_0 - \nabla\phi_1$, where E is the field in the absence of screening and $-\nabla\phi_1$ is the field due to the reorganized charge density. In unitless terms, E_{Tot} is expressed as $E_{\mathrm{Tot}}/E_0 = 1 - \nabla'\psi = 1 + E_1 = \alpha + E_2$. Let $E_{\mathrm{Tot}} = -\nabla V$. Direct integration yields $V = E_0(K_2\rho^{-1}\mathrm{e}^{-\rho x'} - \alpha x' + K_3)$. The user applies a voltage V_{App} to the left electrode and grounds the right, so the boundary conditions for $V(x')$ are

$$V(0) = V_{\mathrm{App}} \quad (10a)$$

and

$$V\left(L'\right) = 0. \quad (10b)$$

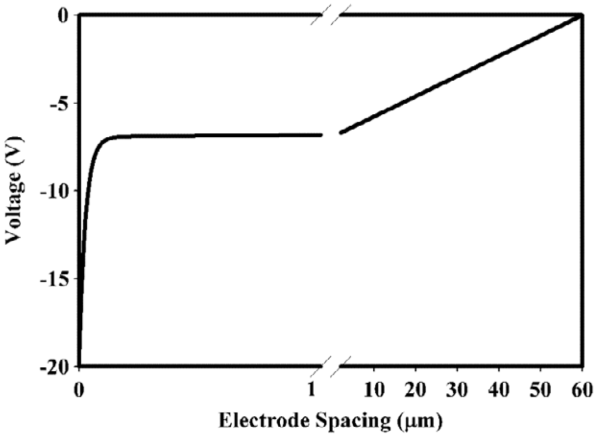

Figure 3. The voltage profile in the solution, calculated via equation (11*b*). For this plot, $V_{\mathrm{App}} = -20$ V, $\alpha = 0.4$ and $(2\gamma)^{-1/2} \sim 30$ nm.

K_2 is found to be $K_2 = \rho(V_{\mathrm{app}} - \alpha L E_0)\mathrm{e}^{\rho L}[E_0(\mathrm{e}^{\rho L} - 1)]^{-1}$, and K_3 is found to be $K_3 = (\alpha L E_0 \mathrm{e}^{\rho L} - V_{\mathrm{App}})/[E_0(\mathrm{e}^{\rho L} - 1)]^{-1}$. The potential $V(x')$ is:

$$V\left(x'\right) = \frac{\alpha V_{\mathrm{App}}\left[\mathrm{e}^{\rho L} + \frac{x'}{L}\left(1 - \mathrm{e}^{\rho L}\right)\right] + (1-\alpha)\, V_{\mathrm{App}}\mathrm{e}^{\rho\left(L - x'\right)} - V_{\mathrm{App}}}{\left(\mathrm{e}^{\rho L} - 1\right)}. \qquad (11a)$$

We show below that $\rho \gg 1$. In this limit where $\mathrm{e}^{\rho L} - 1 \sim \mathrm{e}^{\rho L}$, equation (11*a*) reduces to

$$V\left(x'\right) = \alpha V_{\mathrm{App}}\left(1 - \frac{x'}{L}\right) + (1-\alpha)\, V_{\mathrm{App}}\mathrm{e}^{-\rho x'}. \qquad (11b)$$

This equation indicates that the potential at any point x is composed of two components, one of initial magnitude $V_{\mathrm{App}}(1-\alpha)$ that is screened out across a length scale of ρ^{-1}, and one of initial magnitude αV_{App} that decays across the entire gap. An example of such a partially screened voltage profile is plotted in figure 3. Depending on the magnitude of α, a significant fraction of the applied voltage may extend across the entire gap-length.

4. Results

Figures 1(a) and (b) show that both metallic and polymeric wires grow along the line bridging the biased and grounded electrode tips. Consider the indium wire in figure 1(a). The smooth, near-cylindrical structure of this crystalline-anisotropic material arises through the shape preserving dendritic solidification mechanism. The wire also grows along a predictable vector in the laboratory-reference frame. This latter behavior has nothing to do with dendritic solidification but rather the DENA-process. The amorphous polythiophene wire in figure 1(b) lacks crystalline anisotropy, so dendritic solidification plays no role in its growth [44]. The wire has a knobby structure, not smooth like the indium wire. Shape preserving growth does not occur with amorphous materials. Nevertheless, the aspect ratio of the polymeric structure is $30.2\ \mu\mathrm{m}/0.34\ \mu\mathrm{m} = 89$, reflecting its wire-like shape on the macroscopic scale. Like the metallic wire, the polymeric wire also grows along a predictable vector in the laboratory-reference frame. We hypothesize that control over the growth direction of both metallic and crystalline wires as well as the template-free production of wire-shaped structures from amorphous materials are due to the anisotropic voltage field that is supplied by the DENA technique.

The theoretical analysis of section 3 indicates that *partial* screening of the applied voltage gives rise to a long range voltage component that guides the growth of the wire across the gap to the opposing electrode. To assess the practical magnitude of this component, equation (11*b*) must be evaluated using realistic values for the parameter α, which sets the magnitudes of the drift and screening terms in equation (11*b*). We perform this analysis for indium wire growth, assuming that growth occurs when the system is in a steady state: the cationic flux is uniform across the electrode gap. This assumption is valid when the half-period of the square-wave voltage-signal is much greater than the build-up time for the partial Helmholtz layers. Hence, the flux j_{e} at the electrode–electrolyte interface must equal the flux elsewhere in the solution j_{Drift} that is driven by the field $E_{\mathrm{Drift}} = \alpha V_{\mathrm{App}}/L$. j_{e} describes the deposition that is responsible for wire growth and is given by the mass conservation boundary condition [23]:

$$j_{\mathrm{e}} = v\left(\rho - c_{\mathrm{Int}}\right) \qquad (12)$$

v is the growth velocity of the wire, and ρ is the (number) density of the wire-material, and c_{Int} is the ion concentration on the solution side of the interface. c_{Int} is small compared to ρ. j_{e} is found to be $9.9 \times 10^{11}\ \mu\mathrm{m}^{-2}\ \mathrm{s}^{-1}$ for an indium wire grown with an observed growth velocity of $v = 26\ \mu\mathrm{m\ s}^{-1}$, an applied voltage of $V_{\mathrm{App}} = \pm 20$ V, and $\rho_{\mathrm{In}} = 3.8 \times 10^{10}\ \mu\mathrm{m}^{-3}$ [23]. Invoking the steady-state condition $j_{\mathrm{e}} = j_{\mathrm{Drift}}$ and the relationship $j_{\mathrm{Drift}} = \beta D z e C_0 E_{\mathrm{Drift}} = \beta D z e C_0 \alpha V_{\mathrm{App}}/L$, the parameter α is

$$\alpha = \frac{j_{\mathrm{e}} L}{\beta D z e C_0 V_{\mathrm{App}}}. \qquad (13)$$

α is computed to be 0.75 using the values $\beta = 2.44 \times 10^{8}\ \mathrm{kg}^{-1}\ \mu\mathrm{m}^{-2}\ \mathrm{s}^{2}\ \mathrm{C}$ (for $T = 300$ K), $D = 1000\ \mu\mathrm{m}^{2}\ \mathrm{s}^{-1}$, $z = 3$, $L = 60\ \mu\mathrm{m}$, and $C_0 = 55\ \mathrm{mM} = 3.31 \times 10^{7}\ \mu\mathrm{m}^{-3}$ (as reported elsewhere [23]). Thus, a voltage equal to 75% of V_{App} drops linearly across the gap. The corresponding parameter $(1-\alpha)$ is 0.25. The dashed curve in figure 4 denotes the full voltage profile (i.e. equation (11*b*)) associated with these parameters. The growth velocity determines the size of the long range potential. The dotted profile corresponds to a growth velocity of $13\ \mu\mathrm{m\ s}^{-1}$ for which $\alpha = 0.4$, whereas the solid line corresponds to a growth velocity of $34\ \mu\mathrm{m\ s}^{-1}$ for which $\alpha \sim 1$. For realistic experimental parameters, a significant fraction of V_{App} is not screened but instead extends across the entire electrode gap.

It remains to compute a realistic value for the screening length ρ^{-1} in equation (9*b*). This quantity is given by $\rho^{-1} = (2\gamma)^{-1/2} = [2C_0L^2/(\beta\varepsilon\varepsilon_0 V_{\mathrm{App}}^2)]^{-1/2}$. Using the quantities given above, $\gamma \sim 1.7 \times 10^{3}$, so the approximation of

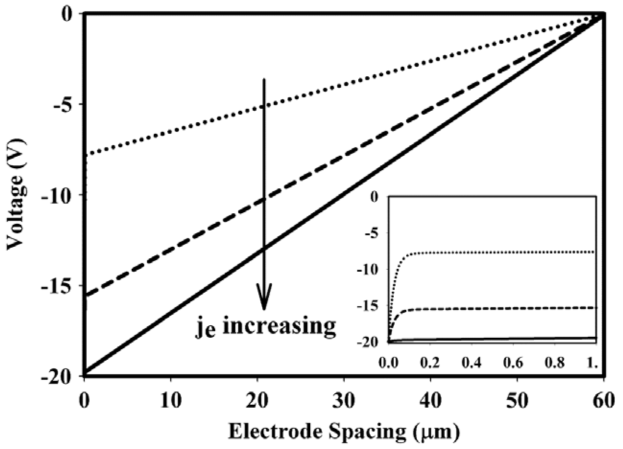

Figure 4. The voltage profiles in the solution, calculated via equation (11*b*). The different profiles correspond to different values of j_e, which sets the parameter α, with j_e increasing in the direction indicated by the arrow.

equation (9*a*) is justified. Furthermore, $\rho^{-1} \sim 0.02$. This short screening length (relative to $x'(L) = 780$) justifies setting A_1 to 0 in equation (9*b*).

Figures 1(a) and (b) depict wire growth to the only other conducting object in the system, consistent with the notion that a long range voltage component defines the growth path. Observing how the wire grows when there are several conducting objects to choose from yields a more detailed description of this behavior: which path does the wire choose? Figure 5(a) depicts a 16-electrode array, where the spacing between the tips of the electrodes varies from 20 μm for a neighboring pair to ~100 μm for two electrodes on opposite sides of the array. Indium wires were grown in this study, as described above. The numbering scheme shown in figure 6(a) is used to refer to the electrodes. In each of the trials depicted in figures 5(a)–(f), a different electrode was grounded while the voltage-signal was applied to electrode 2; nothing was done to the other 14 electrodes. During growth, the drop of solution encompassed all of the electrodes. In the situation depicted in figure 5(a), the wire grew from electrode 2 to 16, even though electrodes 1 and 3 were closer (to electrode 2); the wire did not simply grow to the nearest metallic object. Similar behavior was observed in figures 5(b)–(f). The tip-to-tip distances for these electrode pairs vary from 41.2 μm for pair 2–16 to 94.3 μm for pair 2–11. With reference to the horizontal line connecting electrodes 2 and 11, the path-angle varies from +65° for pair 2–16 to −72° for pair 2–5, demonstrating directional control across a 137° range. The growth path lies within ±3 μm of the straight line connecting the selected pair of electrode tips. Hence, the user may specify the growth path by selection of the biased and grounded electrodes, as the wire grows along the line that connects the tips of these electrodes.

We have employed a finite element analysis routine (FemLab) to calculate the electric potential and the current density in the inter-electrode region of the 16-electrode array. Screening is not included; the aim is to characterize the 2D vector field of electric force components in the inter-electrode region of this 16-electrode array. The inter-electrode medium is described by a uniform dielectric constant. Figure 6(d) is a reproduction of figure 5(d). Figure 6(b) depicts the finite element analysis-based description of this case: −10 V is applied to electrode 2, electrode 7 is grounded, and nothing is done to the remaining 14 electrodes. The equipotential profiles are shown in color and indicate that the voltage increases across the gap from −10 V at electrode 2 to 0 V at electrode 7. Near the electrodes, these contours reflect the electrode-shapes, but in the middle of the gap, the contours are nearly flat. The electric field at a given point is perpendicular to the equipotential profile at that point and is directed towards the negatively biased electrode. These profiles describe a field vector that extends in a straight line from the tip of electrode 7

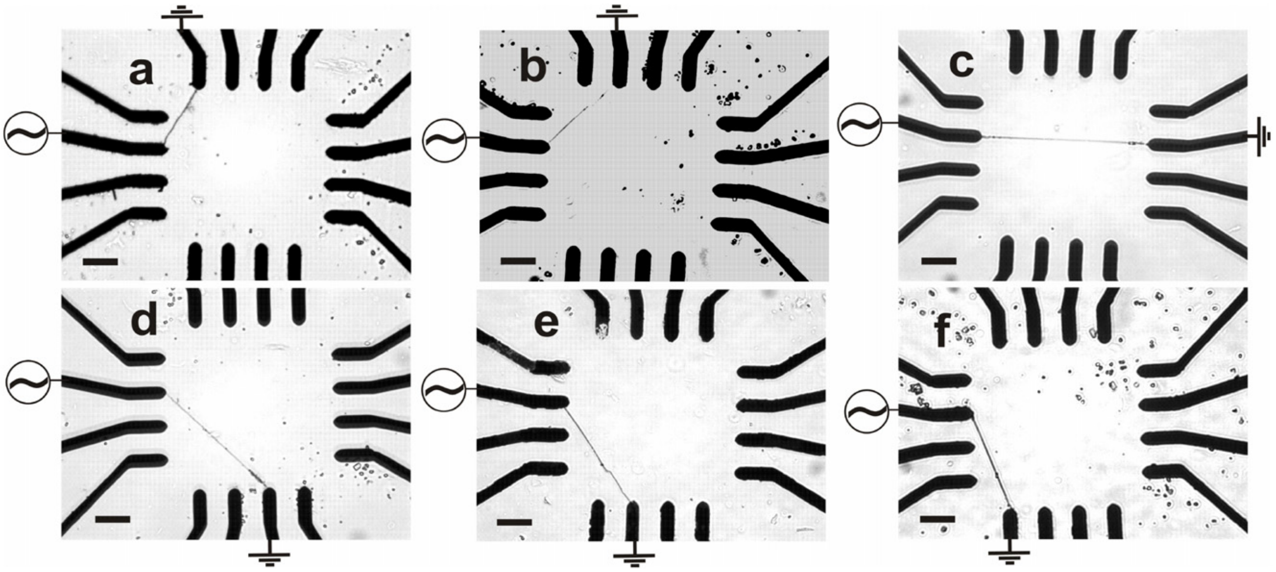

Figure 5. A series of nanowires grown between user-selected electrode pairs. The alternating and grounded electrodes are electrodes (a) 2 and 16, (b) 2 and 15, (c) 2 and 11, (d) 2 and 7, (e) 2 and 6, and (f) 2 and 5, respectively, where the electrode numbering scheme of figure 6(a) was used. The scale bars denote 20 μm.

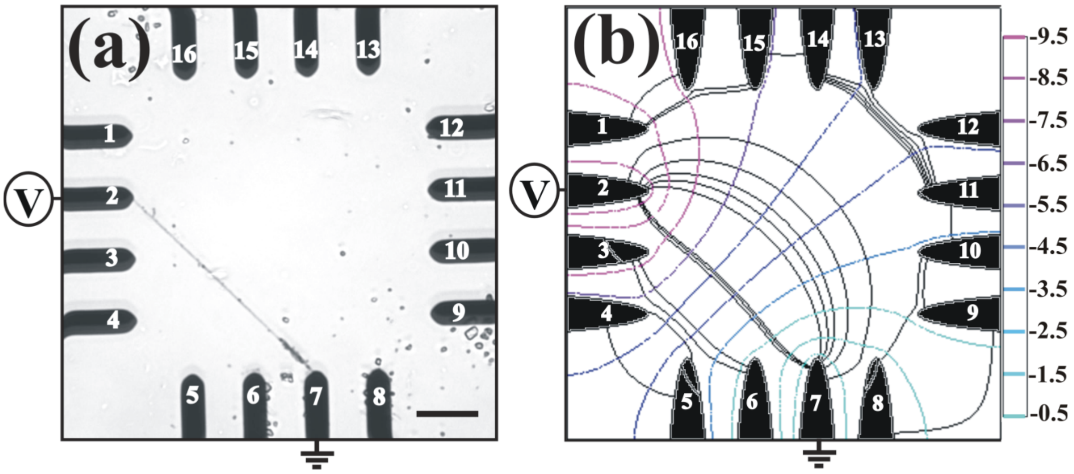

Figure 6. (a) Optical micrograph of a wire grown from electrode 2 to electrode 7 (identical to figure 5(d)). The scale bar represents 20 μm. (b) A numerically calculated map of the electric potential (colored contours) and current density (black contours) on a 16-electrode array when electrode 2 is biased with -10 V and electrode 7 is grounded.

to the tip of electrode 2. This field drives a current density of positive charge along this line towards electrode 2, as indicated by the black equi-current contours. The position of the wire in figure 6(a) is well described by the predicted pathway.

5. Discussion

The DENA technique harnesses dendritic solidification to produce wire-shaped metallic structures, but dendritic solidification alone cannot determine the growth path in the laboratory-reference frame. The possibility remains that an electric field defines the inter-electrode path; however, this cannot occur if there is complete screening of the applied voltage. To assess the extent of screening in our electrochemical cells, we have worked out a theory for the voltage profile in the electrolyte-rich gap. The one-dimensional diffusive model of section 3 demonstrates that the unscreened fraction of V_{App} can be significant: it varies from 40% to 75% of V_{App} across the 13–26 $\mu\mathrm{m\ s}^{-1}$ growth velocity range that is commonly attained during indium wire growth (see figure 4). For the -15.3 V drop that occurs when the wire grows at 26 $\mu\mathrm{m\ s}^{-1}$, the potential to thermal energy ratio is $3e(15.3\ \mathrm{V})/k_{\mathrm{B}}T \sim 1800$, so the voltage is sufficient to overcome thermal motion and transport In^{3+} ions down the voltage gradient. This flux is maximized along the tip-to-tip line, in correspondence with the tip-to-tip growth path that is observed in figure 1(a). The observed paths in the more complex, 16-electrode arrays describe straight lines between the biased and grounded electrode tips. The finite element analysis-based results for this system indicate that a nearly linear ridge of electric field maxima extends between these electrodes. The growth path coincides with this line rather than along any other direction on the 2D array because the flux of particles that feeds the growing wire is maximized along this vector. Indeed, the observed path of figure 6(a) corresponds to the vector of maximum ion-flux in figure 6(b). We conclude that controlling the growth-paths of metallic wires requires *incomplete* screening and, thus, an anisotropic, long range component of the applied voltage-signal to extend through the solution to the targeted electrode.

This anisotropic, long range potential is most crucial to the growth path control of metallic dendrites during the initiation of their growth. Metallic dendrites grow in the direction normal to their high energy-crystallographic plane due to the dendritic solidification mechanism. It is likely, therefore, that the anisotropic voltage selects the nucleation seeds with the correct orientation for long range growth; all others cease to grow much beyond the seed state and, thus, wires that are not aligned with the tip-to-tip path are rarely observed. It should be noted that the electric field determines the growth direction (in the lab frame), but has little effect on the shape of metallic nanowires. This is not the case with polymeric wires, however.

Dendritic solidification plays no role in wire growth from amorphous materials as they lack crystalline anisotropy and, therefore, tend to grow in arbitrary directions or as films [40]. How then does DENA produce wire-like shapes from polymeric materials? Figure 6(b) indicates that a roughly uniform current density flows from electrode 7 to electrode 2 in the region bounded by the innermost pair of equi-current contours. This region may be regarded as an electrical channel. The channel-width determines the precision with which the wire follows the tip-to-tip line. Within this region, the flux is nearly uniform and the wire grows isotropically. Figure 7 depicts a transmission electron micrograph of a ~12 μm length of polypyrrole wire. Its structure is quite knobby. Each knob is the result of a tip-splitting event (during the growth of the wire) after which one tip stopped growing while the other continued. The weaker flux onto one tip slowed its growth relative to the other that received a stronger flux of particles. Thus, the knobby character of a wire reflects both the time-averaged geometry of the channel through which it grows as well as the instantaneous fluctuations of the ion concentration field along its solidification front. As a whole, the segment has a large aspect ratio (~18) that approximates a wire. The diameter of a cylinder encompassing all knobs of this wire would be 1.8 μm,

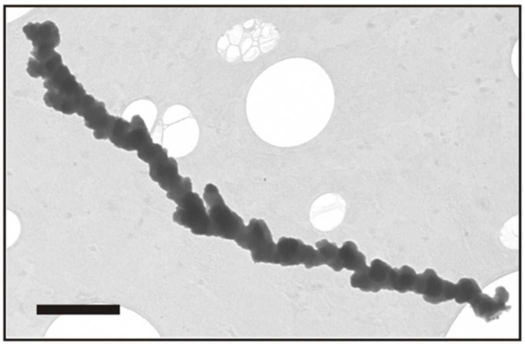

Figure 7. Transmission electron micrograph of a polypyrrole wire, that has been deposited on a holey carbon grid (Ted Pella). The scale bar denotes 2 μm.

suggesting the effective width of this channel. The wire does not grow appreciably outside of this region because the flux falls off outside of this region. Thus, the external field breaks the tendency for isotropic growth by delivering maximal flux along a single direction—the tip-to-tip line. A similar effect has been observed in Hele-Shaw cells—the hydrodynamic analog to diffusion limited growth. An etched line along the bottom plate of a Hele-Shaw cell was observed to induce rapid bubble growth predominantly along the scratch, instead of radially outward without angular preference [37]. The scratch functions as a mechanical channel. The anisotropic field that is applied in the DENA technique is analogous to this scratch. It is also analogous to the mechanical channels that shape and direct the growth of wires in templated growth approaches, yet it does not require prefabrication of the channel-matrix.

6. Conclusion

An anisotropic long range component of the applied voltage extends from the biased to grounded electrode during execution of the DENA technique. This effect has three benefits to nanowire growth. It establishes precise control over the growth path of crystalline metallic nanowires that grow by the dendritic solidification mechanism. It enables the electrochemical polymerization of amorphous polymeric nanowires without the use of mechanical templates. And as with the metallic wires, it establishes control over the polymeric wire growth path.

This on-chip wire growth approach provides a convenient means of characterizing nanowire-transport properties [22]. The range of known DENA-active materials is almost certainly incomplete, suggesting that DENA will enable the fabrication of additional types of wires. One interesting prospect regards the on-chip production biological nanowires, such as the conductive intercellular filaments that integrate *Shewanella oneidensis* colonies [45]. The transport properties of these bio-wires are poorly understood, but attaining this knowledge would provide insight into intercellular electrical communication between single-cellular organisms. Another direction centers on the electrical or chemical induction of surface tension anisotropy during the growth of typically amorphous materials such as conducting polymers. This step could enable the (dendritic) solidification of crystalline polymeric interconnects with dramatically enhanced conductivities.

Acknowledgments

This work was supported by the National Science Foundation (research grant numbers PHY-646966, ECCS-0601362, and EPS-0447262; instrumentation grant numbers DBI-0520678 and EAR-0722410).

Appendix. Shape-preservation in dendritic solidification

The shape preserving growth that is characteristic of dendrites in nature requires the dendrite to grow with a steady velocity and tip radius. A solidification front with a parabolic shape permits this type of stability, whereas flat and spherical fronts typically do not [46]. Indeed, the tips of growing dendrites are observed to be very nearly parabolic. Consider growth due to particle-transport (as in the present study). The parabolic front is stable because transport occurs from the sides as well as the forward direction, so the concentration field around the front is not depleted. Ivantsov established that the product vr of the growth velocity v and the tip radius r of a parabolic dendrite is determined by the experimental parameter Δ which sets the driving force (e.g. applied voltage, undercooling, supersaturation, hydrostatic pressure difference, or combinations thereof) for the solidification process [47]. This result is known as the Ivantsov relation:

$$\Delta = pe^{p}E_1(p) \qquad \text{(A.1)}$$

where, $p = rv/(2D)$ is the Péclet number and $E_1(p)$ is the exponential integral [47, 27, 48–50, 30]. This result permits a continuum of v and r values for a given Δ (one equation, two unknowns). Fixed v and r values are needed for shape preserving growth. Another relationship is needed before v and r may be determined, so the Ivantsov picture is an incomplete description of dendritic solidification [47]. The establishment of a second vr relationship is termed velocity-selection and required nearly a half-century of further work [51].

Shape preserving growth is surprising given the expectation that microscopic deformations of the solidification front will arise due to, say, spatiotemporal fluctuations in the number of solidifying particles on the liquid side of the front. If diffusion to the front were the only important process, these protrusions would grow at amplified rates because—by virtue of extending farther into the solution—the flux onto the protruding tips would be larger than the flux onto the neighboring depressions (the Mullins–Sekerka instability) [52]. Thermal fluctuations cause the tips to split, resulting in highly ramified structures resembling seaweed or fractal aggregates [41, 53, 32, 31]. The surface tension (which determines the capillary length d_0) of the solid–liquid interface counteracts the Mullins–Sekerka instability, so shape preserving growth becomes possible. This factor induces the dissolution of protrusions with large curvature (and large surface-to-volume ratios) in order to minimize the free energy—the Gibbs–Thompson effect [54]. For a protrusion of the right length scale λ_s, the tendency of the Mullins–Sekerka instability to induce runaway growth is precisely balanced by the tendency of the Gibbs–Thompson effect to induce tip-dissolution. In 1978, Langer and Müller-Krumbhaar hypothesized that the operating point of the dendritic tip occurs at this marginally stable point [55–57]. The full theory for this process did not come until nearly a decade later [58, 59, 54].

The surface tension of crystalline materials is anisotropic because different facets have different structures. The form of the diffusion equation that accounts for both the capillary length d_0 and its anisotropy ε reduces to an eigenvalue equation for the parameter σ, which is proportional to the square of the ratio of the stability length scale λ_s to the tip radius [39]:

$$\sigma = \left(\frac{\lambda_s}{2\pi r}\right)^2. \qquad \text{(A.2}a\text{)}$$

The only solution for σ that is consistent with shape preserving growth is [58]

$$\sigma^* = \sigma_0 \varepsilon^{7/4}, \qquad \text{(A.2}b\text{)}$$

where σ_0 is roughly unity. If there is no crystalline anisotropy ($\varepsilon = 0$), shape preserving growth is impossible and dendritic solidification does not occur. The observed interface has a tip radius that scales inversely with $\varepsilon^{7/4}$ [58]. Dendrites grow fast and thin (large ε) or slow and thick (small ε), so the balance between the area of the high energy-tip and the area of the lower energy sides is set by ε. The shape of the dendrite is stable against environmental fluctuations. If r becomes much greater than λ_s, protrusions of a size λ where $r > \lambda \sim \lambda_s$ will develop along the front. A protrusion centered on the tip grows fastest due to ε. The Gibbs–Thompson effect dissolves those on the sides that do not grow as fast. Only the forward directed lobe of size $\lambda \sim \lambda_s$ survives. Thus, r is reduced and the equality between r and λ_s is restored. If r becomes smaller than λ_s, the Gibbs–Thompson effect intensifies at the high curvature tip, slowing its growth and increasing r. A shape preserving needle-shaped dendrite results. If the deformation amplitude is comparable to r, the dendrite will develop a deformation. Because the material grows fastest in the direction normal to its high energy surface, these protrusions are convected downward (becoming side-branches) and the tip remains stable [46]. A tree-shaped deposit results. Equations (A.1), (A.2*a*) and (A.2*b*) accurately predict unique values for v and r (two equations, two unknowns) [51], so equation (2) is called the *microscopic solvability condition*. DENA harnesses dendritic solidification to produce near single crystalline needle-shaped structures from metallic materials that are useful as current carrying wires [22].

References

[1] Wirtz M and Martin C R 2003 Template-fabricated gold nanowires and nanotubes *Adv. Mater.* **15** 455–8

[2] Ramanathan K, Bangar M A, Yun M, Chen W, Myung N V and Mulchandani A 2005 Bioaffinity sensing using biologically functionalized conducting-polymer nanowire *J. Am. Chem. Soc.* **127** 496–7

[3] Woodsen M and Liu J 2006 Guided growth of nanoscale conducting polymer structures on surface-functionalized nanopatterns *J. Am. Chem. Soc.* **128** 3760–3

[4] Wong T C, Li C P, Zhang R Q and Lee S T 2004 Gold nanowires from silicon nanowire templates *Appl. Phys. Lett.* **84** 407–9

[5] Bezryadin A, Westervelt R M and Tinkham M 1999 Self-assembled chains of graphitized carbon nanoparticles *Appl. Phys. Lett.* **74** 2699–701

[6] Hermanson K D, Lumsdon S O, Williams J P, Kaler E W and Velev O D 2001 Dielectrophoretic assembly of electrically functional microwires from nanoparticle suspensions *Science* **294** 1082–6

[7] Kretschmer R and Fritzsche W 2004 Pearl chain formation of nanoparticles in microelectrode gaps by dielectrophoresis *Langmuir* **20** 11797–801

[8] Ozturk B, Talukdar I and Flanders B N 2005 The directed-assembly of CdS interconnects between targeted points in a circuit *Appl. Phys. Lett.* **86** 183105

[9] Ozturk B, Blackledge C, Grischkowsky D R and Flanders B N 2006 Reproducible interconnects assembled from gold nanorods *Appl. Phys. Lett.* **88** 073108

[10] Wagner R S and Ellis W C 1964 Vapor–liquid–solid mechanisms of single crystal growth *Appl. Phys. Lett.* **4** 89–90

[11] Huang M H, Mao S, Feick H, Yan H, Wu Y, Kind H, Weber E, Russo R and Yang P 2001 Room-temperature ultraviolet nanowire nanolasers *Science* **292** 1897–9

[12] Aleshin A N, Lee H J, Park Y W and Akagi K 2004 One-dimensional transport in polymer nanofibers *Phys. Rev. Lett.* **93** 196601

[13] Rahman A and Sanyal M K 2007 Observation of charge density wave characteristics in conducting polymer nanowires: possibility of Wigner crystallization *Phys. Rev.* B **76** 045110

[14] Kemp N T, McGrouther D, Cochrane J W and Newbury R 2007 Bridging the gap: polymer nanowire devices *Adv. Mater.* **19** 2634–8

[15] Fan Y, Chen X, Trigg A D, Tung C, Kong J and Gao Z 2007 Detection of microRNAs using target-guided formation of conducting polymer nanowires in nanogaps *J. Am. Chem. Soc.* **129** 5437–43

[16] Richardson-Burns S M, Hendricks J L and Martin D C 2007 Electrochemical polymerization of conducting polymers in living neural tissue *J. Neural Eng.* **4** L6–13

[17] Richardson-Burns S M, Hendricks J L, Foster B, Povlich L K, Kim D H and Martin D C 2007 Polymerization of the conducting polymer poly(3,4-ethylenedioxythiophene) (PEDOT) around living neural cells *Biomaterials* **28** 1539–52

[18] Das A, Lei C H, Elliot M, Macdonald J E and Turner M L 2006 Non-lithiographic fabrication of PEDOT nano-wires between fixed Au electrodes *Org. Electron.* **7** 181–7

[19] Noy A, Miller A E, Klare J E, Weeks B L, Woods B W and DeYoreo J J 2002 Fabrication of luminescent nanostructures and polymer nanowires using dip-pen nanolithography *Nano Lett.* **2** 109–12

[20] Thapa P S, Barisci J N, Yu D J, Wicksted J P, Baughman R and Flanders B N 2009 Directional growth of conducting polypyrrole and polythiophene nanowires *Appl. Phys. Lett.* **94** 033104

[21] Talukdar I, Ozturk B, Mishima T D and Flanders B N 2006 Directed growth of single crystal indium wires *Appl. Phys. Lett.* **88** 221907

[22] Ozturk B, Mishima T, Grischkowsky D R and Flanders B N 2007 Single step growth and low resistance interconnecting of gold nanowires *Nanotechnology* **18** 175707

[23] Ozturk B, Talukdar I and Flanders B N 2007 Directed growth of diameter-tunable nanowires *Nanotechnology* **18** 365302

[24] Cheng C, Gonela R K, Gu Q and Haynie D T 2005 Self-assembly of metallic nanowires from aqueous solution *Nano Lett.* **5** 175–8

[25] DeMarzi G, Iacopino D, Quinn A J and Redmond G 2004 Probing intrinsic transport properties of single metal nanowires: direct-write contact formation using a focused ion beam *Appl. Phys. Lett.* **96** 3458–62
[26] Huang S C and Glicksman M E 1981 Fundamentals of dendritic solidification—II Development of sidebranch structure *Acta Metall.* **29** 717–34
[27] Huang S C and Glicksman M E 1981 Fundamentals of dendritic solidification *Acta Metall.* **29** 701–15
[28] Langer J S 1980 Instabilities and pattern formation in crystal growth *Rev. Mod. Phys.* **52** 1–28
[29] Glicksman M E, Shaefer R J and Ayers J D 1976 *Metall. Trans.* A **7** 1747–59
[30] Dougherty A and Gollub J P 1988 Steady-state dendritic growth of NH_4Br from solution *Phys. Rev.* A **38** 3043–53
[31] Sawada Y, Dougherty A and Gollub J P 1986 Dendritic and fractal patterns in electrolytic metal deposits *Phys. Rev. Lett.* **56** 1260–3
[32] Grier D, Ben-Jacob E, Clarke R and Sander L M 1986 Morphology and microstructure in electrochemical deposition of zinc *Phys. Rev. Lett.* **56** 1264–7
[33] Kepler J *1611 De Nive Sexangula (Original)* (Frankfurt am Main: Godfrey Tampach)
[34] Kepler J 1966 *The Six-Cornered Snowflake* (Oxford: Clarendon) (translation by C Hardie)
[35] Libbrecht K G and Tanusheva V M 1999 Cloud chambers and crystal growth: effects of electrically enhanced diffusion on dendrite formation formation from neutral molecules *Phys. Rev.* E **59** 3253–61
[36] Libbrecht K 2006 *Field Guide to Snowflakes* (St Paul: Voyageur Press)
[37] Matsushita M and Yamada H 1990 Dendritic growth of single viscous finger under the influence of linear anisotropy *J. Cryst. Growth* **99** 161–4
[38] Langer J S 1989 Dendrites, viscous fingers, and the theory of pattern formation *Science* **243** 1150–6
[39] Barbieri A, Hong D C and Langer J S 1987 Velocity selection in the symmetric model of dendritic crystal growth *Phys. Rev.* A **35** 1802–8
[40] Paterson L 1981 Radial fingering in a Hele Shaw cell *J. Fluid Mech.* **113** 513–29
[41] Hwang R Q, Schroder J, Gunther C and Behm R J 1991 Fractal growth of two-dimensional islands: Au on Ru(0001) *Phys. Rev. Lett.* **67** 3279–82
[42] Bockris J and Reddy A K N 1973 *Modern Electrochemistry* (New York: Plenum)
[43] Nelson P 2004 *Biological Physics* (New York: Freeman)
[44] Brener E A and Mel'nikov V I 1991 Pattern selection in two-dimensional dendritic growth *Adv. Phys.* **40** 53–97
[45] Gorby Y A *et al* 2006 Electrically conductive bacterial nanowires produced by *Shewanella oneidensis* strain MR-1 and other microorganisms *Proc. Natl Acad. Sci.* **103** 11358–63
[46] Saito Y 1996 *Statistical Physics of Crystal Growth* (River Edge, NJ: World Scientific)
[47] Ivantsov G P 1947 Temperature field around spherical, cylindrical and needle-shaped crystals which grow in supercooled melt *Dokl. Akad. Nauk SSSR* **58** 567
[48] Muschol M, Liu D and Cummins H Z 1992 Surface-tension-anisotropy measurements of succinonitrile and pivalic acid: comparison with microscopic solvability theory *Phys. Rev.* A **46** 1038–50
[49] Franck J P and Jung J 1986 Dendritic crystal growth in pure helium-4 *J. Low Temp. Phys.* **64** 165–86
[50] Liu J M 1995 *In-situ* observations of dendritic growth of ammonium chloride crystals from an aqueous solution system *Scr. Metall. Mater.* **32** 445–50
[51] Karma A and Rappel W J 1996 Numerical simulation of three-dimensional dendritic growth *Phys. Rev. Lett.* **77** 4050–3
[52] Mullins W W and Sekerka R F 1964 Stability of a planar interface during solidification of a dilute binary alloy *J. Appl. Phys.* **35** 444–51
[53] Saito Y, Goldbeck-Wood G and Müller-Krumbhaar H 1987 Dendritic crystallization: numerical study of the one-sided model *Phys. Rev. Lett.* **58** 1541–3
[54] Kessler D A, Koplik J and Levine H 1988 Pattern selection in fingered growth phenomena *Adv. Phys.* **37** 255–339
[55] Langer J S and Müller-Krumbhaar H 1978 Theory of dendritic growth—I. Elements of a stability analysis *Acta Metall.* **26** 1681–7
[56] Langer J S and Müller-Krumbhaar H 1978 Theory of dendritic growth—II. Instabilities in the limit of vanishing surface tension *Acta Metall.* **26** 1689–95
[57] Langer J S and Müller-Krumbhaar H 1978 Theory of dendritic growth—III. Effects of surface tension *Acta Metall.* **26** 1697–708
[58] Langer J S 1987 *Chance and Matter* ed J Souletie *et al* (Amsterdam: North-Holland) pp 629–711
[59] Langer J S 1992 Issues and opportunities in materials research *Phys. Today* **45** (October) 24–31